Journal of Applied Research and Technology

www.jart.icat.unam.mx

ICAT Instituto de Ciencias Aplicadas y Tecnología

Journal of Applied Research and Technology 24 (2026) 509-523

Original

Topology Optimized Lattice Design and Mechanical Evaluation of 3D Printed PLA Specimens under Tensile and Compressive Conditions

Alfonso Monzamodeth Román-Sedano [1*] • Osvaldo Flores [2]
Fermín Castillo [2] • Bernardo Hernández-Morales [3]
Bernardo Campillo [3], and Gonzalo González [1*]

[1]Instituto de Investigaciones en Materiales, Universidad Nacional Autónoma de México, Mexico City, Mexico
[2]Instituto de Ciencias Físicas, Universidad Nacional Autónoma de México, Cuernavaca, Morelos, Mexico
[3]Facultad de Química, Universidad Nacional Autónoma de México, Mexico City, Mexico

Received: 27 06 2024; Accepted: 27 04 2025
Available: 30 04 2026

Abstract: The lightweight design of 3D-printed polylactic acid (PLA) components requires optimization strategies that reduce material usage while preserving mechanical performance under loading conditions. In this study, cubic lattice topology optimization was applied to tensile and compression specimens manufactured by 3D printing using PLA. The mechanical properties of the base material were experimentally determined and incorporated into finite element analyses. The boundary conditions were defined to reproduce the experimental stress state under standardized testing, with tensile and compressive loads selected based on the material's yield strength. The optimized geometries were subsequently fabricated by 3D printing and mechanically tested. A qualitative agreement was observed between the simulated and experimental responses, confirming that the gradient-driven optimization approach implemented in ANSYS provided physically representative and experimentally validated designs. The printed PLA

*Corresponding author.
E-mail address: joseggr@unam.mx (Ivan Mendoza-Bravo).
Peer Review under the responsibility of Universidad Nacional Autónoma de México.

exhibited ductile-like behavior attributed to the fused deposition modeling process. Thus, this work demonstrates the feasibility of integrating topology optimization, finite element analysis, and experimental validation to develop PLA components under realistic loading conditions.

Keywords: **3D printing, finite element analysis, lattice topology optimization, mass retention constraint, tensile and compression tests.**

1. Introduction

Additive manufacturing has been widely employed to produce designs with specific features and unique geometries. This method is particularly convenient for fabricating prototypes, decorative objects, and mechanical components that are otherwise expensive to manufacture using conventional methods (León-Becerra et al., 2021; Monzamodeth et al., 2021, 2022). In this regard, three-dimensional (3D) printing is a well-established manufacturing technique applicable to a wide range of materials, including polymers, metals, and ceramics.

In particular, the use of polylactic acid for rapid prototyping has proven highly advantageous, with applications ranging from biomechanical prosthetic devices and aerodynamic models to teaching aids, protective masks, face shields, and topology optimization studies (Monzamodeth et al., 2021, 2022). Moreover, PLA is biodegradable and readily available at a low cost. In topology optimization, 3D printing has enabled the design of mechanical components by allowing the use of various lattice configurations, shapes, and optimization parameters. The primary objective of topology optimization is to minimize the mass or volume of a structure while preserving its mechanical strength under given boundary and environmental conditions (Park et al., 2022; Hooshmand et al., 2023; Gavazzoni et al., 2021; Yang et al., 2025; Mahapatra et al., 2025). For this purpose, parameters such as fabrication geometry, lattice pattern, unit-cell size, and wall thickness are typically investigated and optimized.

Among lattice configurations, cubic structures are the most common, including the simple cubic, face-centered cubic (FCC), body-centered cubic (BCC), and diamond structures. The combination of additive manufacturing and lattice-based topology optimization has enabled numerous studies involving different materials and 3D printing techniques (Mahapatra et al., 2025; Xu et al., 2023; Teng et al., 2022; Bedoya et al., 2025; Raja et al., 2022; Abeykoon et al., 2020). Therefore, continued research on lattice patterns, process parameters, and material performance is essential for understanding optimized mechanical behavior.

In this study, the mechanical properties of tensile and compression specimens fabricated by 3D printing with PLA were evaluated under two conditions: standard (100% infill) and lattice topology optimized. The optimized tensile and compression specimens were obtained through finite element simulations using boundary conditions consistent with those applied in the experimental mechanical tests, with a prescribed 50% mass retention. The resulting geometries were 3D printed, mechanically tested under tension and compression, and subsequently validated by simulation. Comparable behavior was observed between the FEA predictions and experimental results. In particular, the compression specimens exceeded the simulated maximum load. In contrast, the tensile specimens showed an approximate 50% decrease in mechanical properties, directly corresponding to the imposed mass-retention constraint.

2. Materials and Methods

2.1 Topology Optimization Methodology

A strategy was developed to examine differences between the mechanical responses obtained experimentally and those predicted by FEA for tensile and compression specimens. The process began with characterizing the mechanical properties of the base material (PLA). Subsequently, the boundary conditions were defined in ANSYS Mechanical (2025 R1) to reproduce the experimental stress state of the specimens and to determine the distributions of equivalent stress and safety factors. For the present analysis, the safety factor was estimated using the maximum equivalent stress criterion as $SF = \sigma_{Allowable\ Stress}/\sigma_{vM}$. Prior to the simulations, mesh quality was assessed for all numerical models using appropriate indicators for each mesh type. This procedure was conducted to evaluate the structural performance and to analyze

the behavior of the specimens under both standard and topology-optimized configurations. Finally, the differences between the standard and optimized geometries were assessed by comparing simulated and experimental results. A schematic flowchart summarizing the experimental and numerical workflow is presented in Figure 1.

2.2 Manufacturing and Evaluation of Tensile and Compression Specimens

The first step involved determining the mechanical properties of the material used in this study, specifically a commercial gray polylactic acid. This characterization was important for enhancing the accuracy of the finite element simulations and the subsequent topology optimization process. A commercially available gray PLA filament with a nominal diameter of 1.75 mm was used in this study, and an Ender-3 Creality 3D printer was employed. The geometries were processed in the Standard Tessellation Language (STL) format, and the corresponding G-code was generated using the open-source software Repetier Host. Figure 2 shows the geometries and sketches of both designs. The 3D printing parameters were maintained constant throughout all prints: nozzle temperature = 195 ± 3 °C, nozzle diameter = 0.4 mm, heated-bed temperature = 55 ± 2 °C, and printing speed = 50 mm/s. The 3D printing process of the specimens was performed with a nominal infill density of 100%. Under the Repetier Host slicing configuration used in this work, this condition corresponded to a filled internal region rather than to a conventional sparse infill pattern.

On the other hand, tensile specimens were designed in accordance with ASTM D-638, whereas the compression specimens consisted of 50 mm cubic samples defined for comparative compression testing under the selected loading conditions. The samples were labeled as follows: non-optimized tensile specimens (TS) and non-optimized compression specimens (CS). Three non-optimized tensile specimens, labeled TS-1, TS-2, and TS-3, were tested under the same experimental conditions, and the corresponding stress-strain curves are shown in Figure 3(a). The tensile mechanical properties reported in this study were obtained from the average response of these three curves. Moderate differences were observed in the peak stress, strain at maximum stress, and post-peak response. These variations were attributed to specimen-to-specimen variability inherent to fused deposition modeling. Figure 3(b) presents the response of a single compression specimen.

Additional compression tests were not available within the scope of the present study. Tensile and compression tests were performed on an Instron 4206 universal testing machine at a crosshead speed of 0.5 mm/min. Mechanical properties of PLA were then extracted and subsequently implemented in the FEA simulations. The corresponding results are summarized in Table 1. It is important to note that Poisson's ratio was experimentally determined because the assessed material exhibited a ductile-like response. The transverse and longitudinal deformations observed in the tensile and compression specimens are shown in Figure 3c. While PLA is typically reported to have a Poisson's ratio of ≈0.33, characteristic of brittle polymers, the measured value was 0.48, indicating higher deformability and energy absorption. This behavior directly influenced numerical modeling; therefore, the von Mises stress was used instead of the Rankine criterion (commonly applied to brittle materials). Under these conditions, an equivalent-stress criterion based on distortion energy was considered a more suitable engineering approximation than the Rankine criterion, which is associated with failure governed by maximum principal tensile stress.

2.3 Meshing and Boundary Conditions for Tensile and Compression Specimens

Due to the simple geometry of the non-optimized tensile and compression specimens, a structured mesh was generated in both cases. The average element size was 0.5 mm for the non-optimized tensile specimen model and 1mm for the non-optimized compression specimen, resulting in average orthogonal quality values of ≈ 0.99. The total number of elements was 3.76×10^4 for the tensile model and 1.25×10^5 for the compression model.

Regarding the boundary conditions, a uniaxial tensile load of 500 N was applied to the tensile specimen along the loading axis, as shown in Figure 4(a). Fixed supports were assigned at the grip regions to reproduce the constraints imposed by the tensile testing setup. For the compression specimen, a compressive load of 1×10^4 N was applied on the top face, whereas the bottom face was fully constrained, reproducing the experimental compression conditions, as shown in Figure 4(b). These loading magnitudes were selected to approximate the stress states observed experimentally, i.e., for the tensile sample (≈16 MPa), consistent with the experimental yield stress, whereas for the compression cube (≈4 MPa), within the linear-elastic regime of PLA. This ensured that the

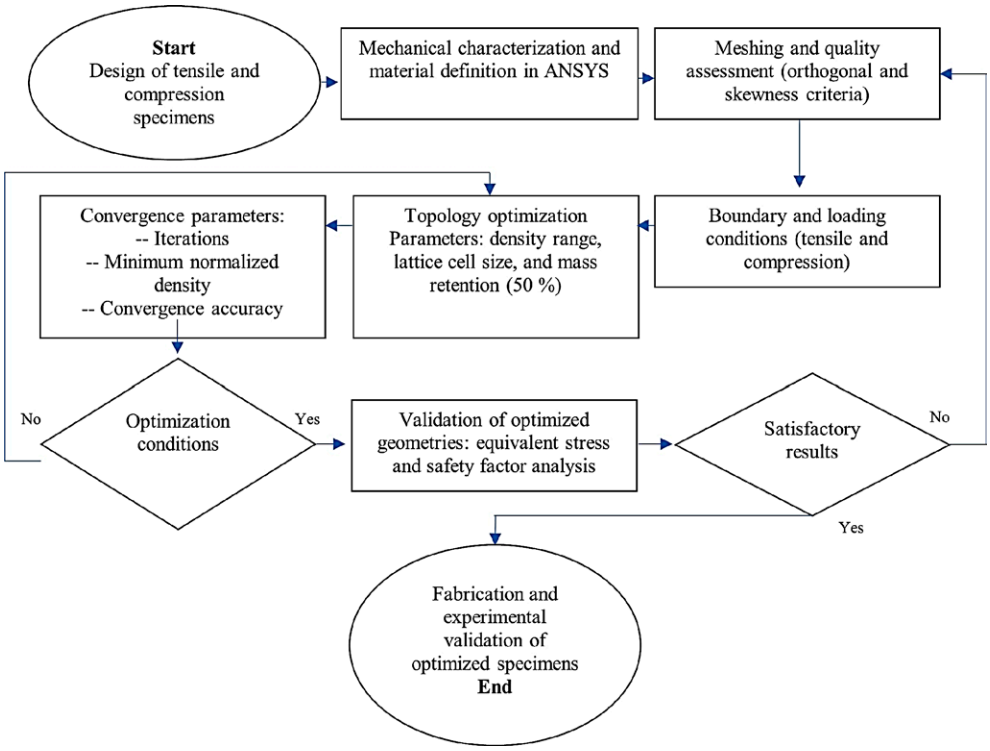

Figure 1. Lattice topology optimization flow chart.

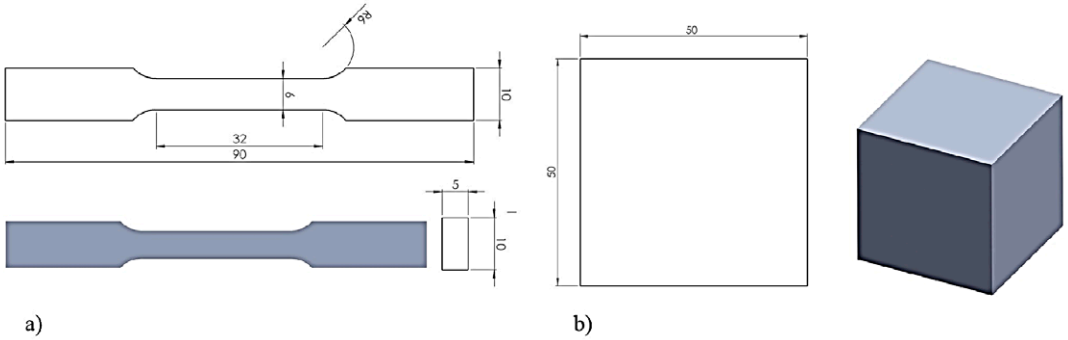

Figure 2. Engineering drawing of samples for mechanical testing. a) Tensile and b) Compression (units in mm).

simulated stresses were physically representative of the mechanical tests and suitable for topology optimization.

The computational modeling was performed under the assumption of isotropic linear-elastic behavior, isothermal conditions, and a global Cartesian coordinate system. The governing equations and constitutive relations have been reported in previous works (Monzamodeth et al., 2021, 2022).

3. Results

3.1 Equivalent Stress and Safety Factors of Non-optimized Tensile and Compression Specimens

Figures 5 and 6 present the finite element results for the tensile and compression specimens, respectively. The simulated response of the tensile specimens revealed safety factor values ≤ 2 in the narrow section of

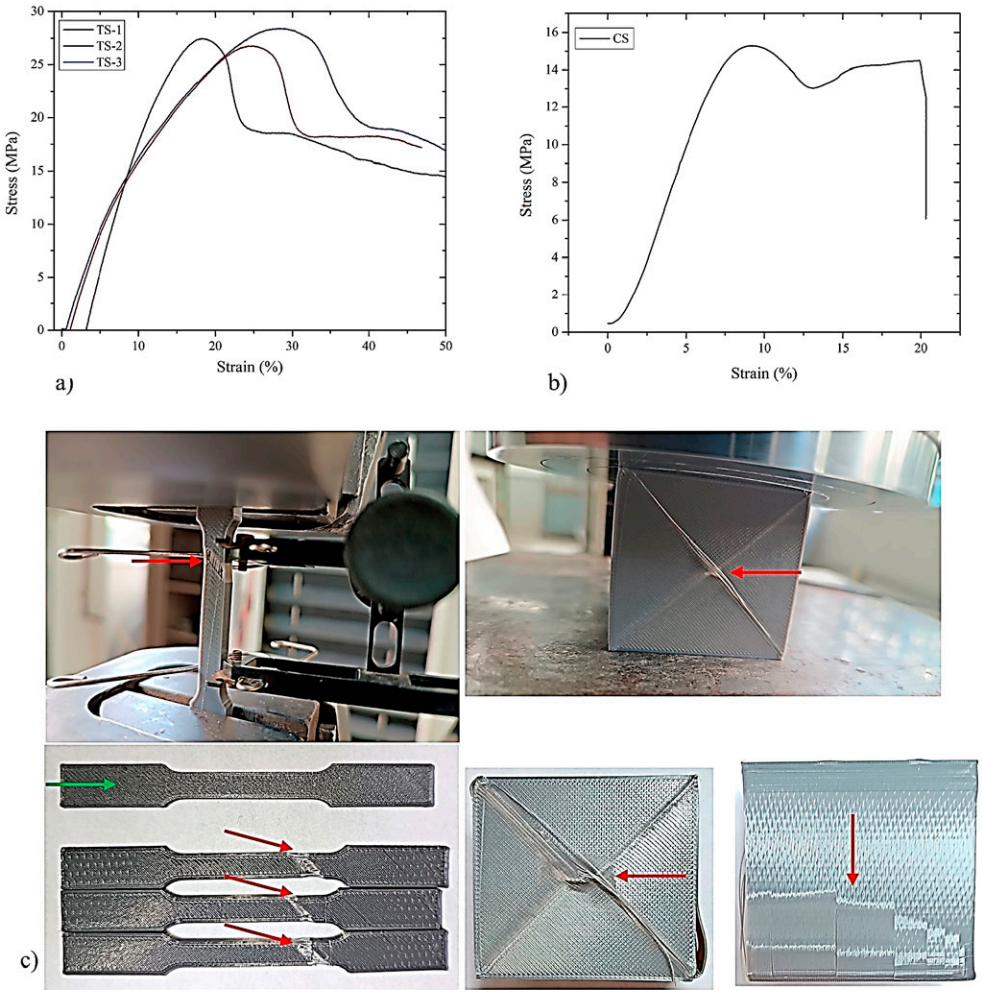

Figure 3. Stress-strain curves. a) Non-optimized tensile sample, b) non-optimized compression sample, and c) localization of deformations and fractures in tested samples. Red arrows indicate the deformed areas; the green arrow points to a tensile specimen that was not tested for comparison.

Table 1. Mechanical properties of tensile and compression specimens.

	Young´s modulus (GPa)	Ultimate tensile strength (MPa)	Compressive strength (MPa)	Tensile Yield strength (MPa)	Compressive Yield Strength (MPa)	Poisson's ratio
Tensile	0.21214	27.5	--	16.2	--	0.48
Compression	0.21924	--	15.28	--	14.8	

the sample, as illustrated in Figures 5a and 5b. From a mechanical design perspective, these values are slightly above the minimum admissible limit, suggesting that localized plastic deformation could occur under the applied 500 N load. The maximum equivalent stress was concentrated in the central region, in agreement with the experimentally observed strain localization. Overall, the numerical predictions showed good consistency with the experimental results, confirming that the applied boundary conditions accurately reproduced the actual testing conditions.

On the other hand, the compression specimens exhibited a stable mechanical response under a $1x10^4$ N load, with a minimum safety factor of approximately 2.5, near

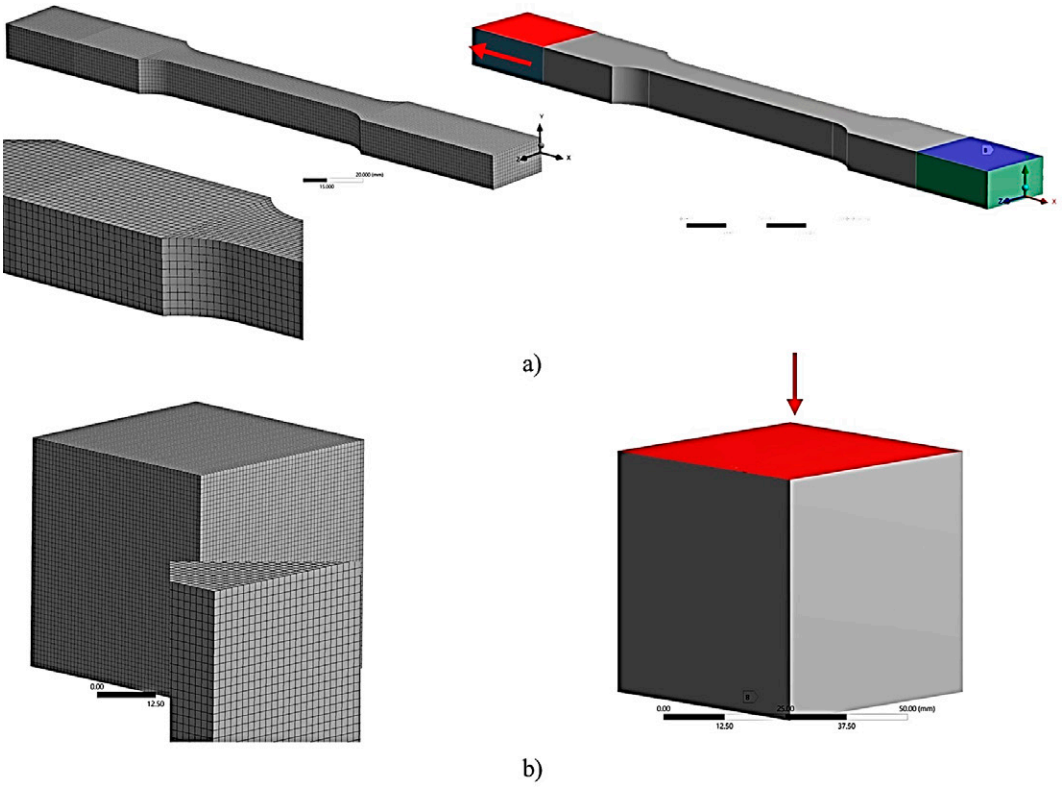

Figure 4. Finite element models and boundary conditions used in the simulations. a) Non-optimized tensile specimen and b) non-optimized compression specimen. For both cases, the figures show the mesh, fixed support regions, and the applied tensile and compressive loads, respectively.

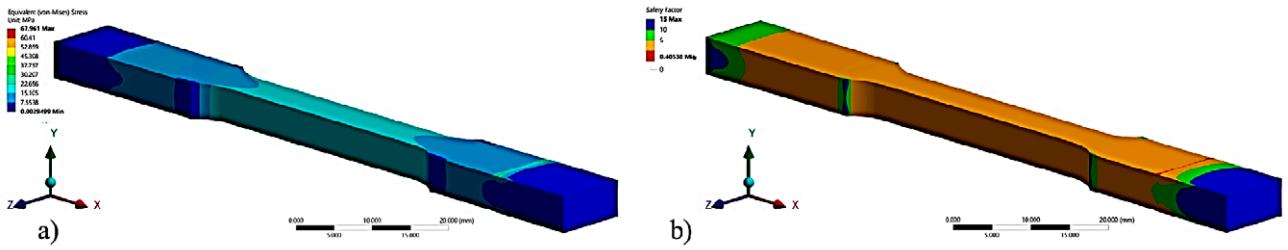

Figure 5. Tensile FEA results. a) Equivalent stress and safety factor (maximum equivalent stress).

the lower support area (Figures 6a and 6b). These results indicated that the compressive configuration remained well within the elastic zone, consistent with the experimental findings.

Based on these observations, the topology optimization stage was subsequently implemented using the validated boundary and material conditions. This ensured that the optimization process would originate from physically representative stress states and produce reliable predictions for the mass-reduced geometries.

3.2 Lattice Topology Optimization

Based on the results discussed above, lattice topology optimization was performed under a fixed mass-retention constraint of 50% relative to the initial mass of each specimen. The optimization procedure was carried out in ANSYS Mechanical (2025 R1) using the Solid Isotropic Material with Penalization method. In this approach, each finite element was assigned a density variable and updated through the optimality criteria algorithm to minimize structural compliance while satisfying the imposed

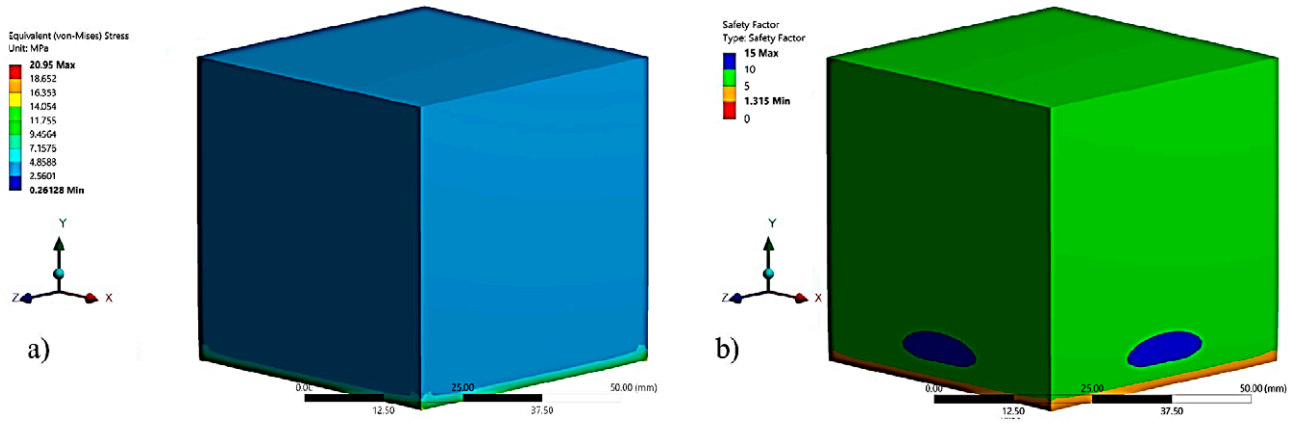

Figure 6. Compression FEA results. a) Equivalent stress and b) safety factor (maximum equivalent stress).

mass constraint. A penalization factor of 3 was applied to suppress intermediate densities and ensure a clearer separation between solid and void regions. Therefore, the 50% mass-retention condition refers here to a target final material fraction equal to one-half of the original mass of the optimization region. The final configuration parameters used to obtain the optimized geometries were as follows: convergence accuracy of 0.1%, minimum normalized density of 1×10^{-3}, maximum number of iterations of 500, and density limits of 0.8 (maximum) and 0.2 (minimum) in the optimization regions. The lattice cell size was set to 5 mm for the tensile specimens and 10 mm for the compression specimens, both adopting a body-centered cubic (BCC) cell. The topology-optimized lattice geometries were maintained in the same global orientation during simulation and fabrication so that the numerical boundary conditions, the printed architecture, and the experimental load path remained consistent. This criterion was adopted to enable a comparison between the tensile and compressive responses under equivalent structural conditions. The selected BCC orientation was particularly favorable under compressive loading, where the lattice members provided more direct load-transfer paths, whereas under tensile loading, the same architecture could remain more sensitive to local stress concentrations in thin load-bearing regions.

The optimization domains, highlighted in blue in Figure 7a, were defined based on the regions of maximum strain energy identified in the preliminary FEA. The resulting density distributions, corresponding to the optimized lattice structures, are shown in Figure 7b.

The optimized configurations revealed a clear redistribution of material toward the load-bearing regions, reducing redundant volume in low-stress areas while preserving the global stiffness of the structure. This redistribution is characteristic of minimum-compliance solutions obtained through gradient-based topology optimization. The expected result is a moderate reduction of the local safety factors (typically between 0.5 and 2) due to the concentration of stresses in the thinner lattice truss, while maintaining overall load-bearing capacity. The optimized models were subsequently exported for further FEA validation, G-code generation, and 3D printing fabrication.

3.3 Tensile and Compression Tests for the Optimized Lattice Geometries

Using the density distributions obtained from the topology optimization (Figure 7b), the optimized geometries were processed by assigning the corresponding density attributes to each region. A uniform wall thickness of 0.3 mm was applied to both specimen types to facilitate geometry reconstruction for meshing and simulation, as well as for generating G-codes and 3D printing. An exhaustive inspection of the 3D models was performed to identify and eliminate any geometric inconsistencies that could compromise either the fabrication or the later FEA validation. The resulting CAD models are shown in Figures 8a and 9a, while the corresponding meshes are presented in Figures 8b and 9b. Due to the complexity of the lattice geometry, an unstructured mesh was employed. For the tensile specimens, the average element size was 0.3 mm, with an average skewness value of 0.34 ±0.22, and a total of $\approx 9.4 \times 10^5$ elements. For the compression specimens, the corresponding values were 1 mm, 0.61 ± 0.24, and $\approx 1.5 \times 10^6$ elements, respectively. The meshing quality ensured adequate representation of the thin lattice truss and avoided distortion during the FEA. The

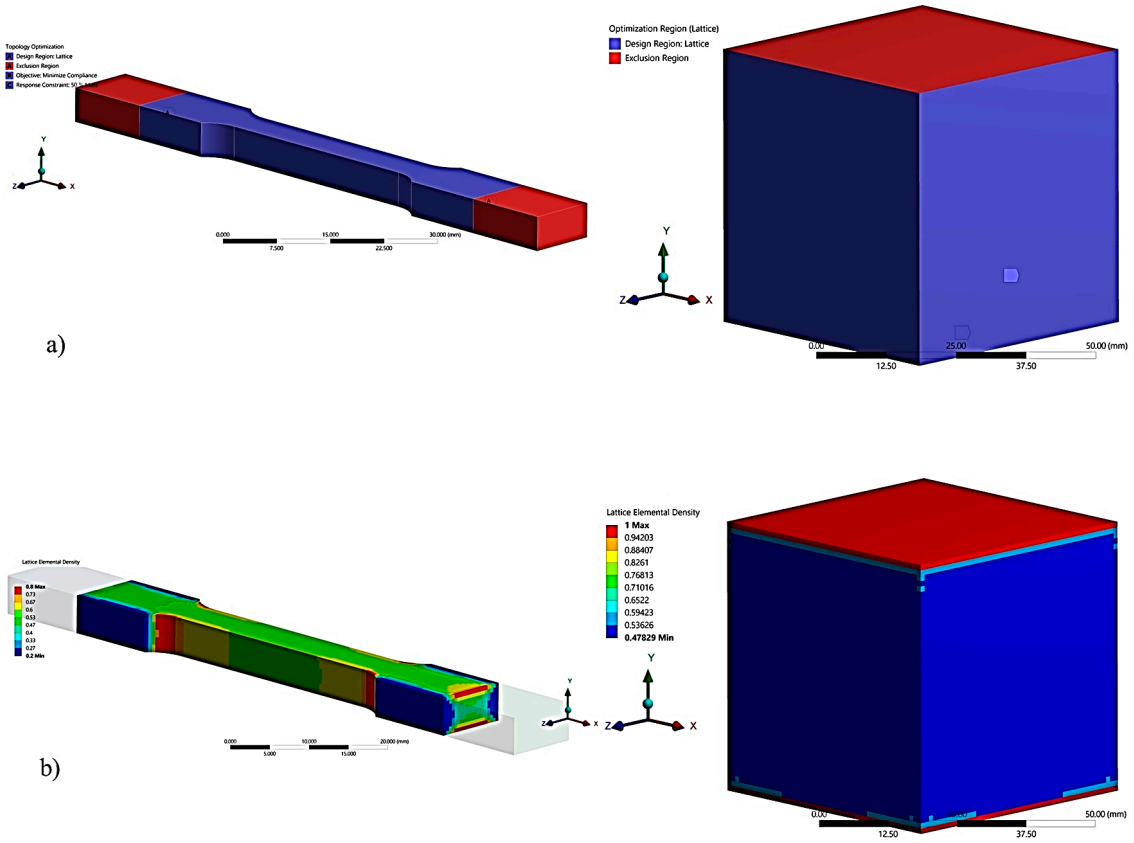

Figure 7. Topology optimization results for tensile and compression specimens.
a) Optimization regions and b) lattice elemental density.

manufacturing process was conducted under the same operating conditions used for the non-optimized specimens. Representative layers of the G-code are shown in Figures 8c and 9c.

Figures 8d and 9d present different views of the fabricated tensile and compression specimens, respectively, in which the BCC lattice topology is clearly visible, consistent with the density distribution predicted during the optimization process. The printed specimens were tested under the same conditions as the non-optimized samples using the tensile testing equipment, and the resulting stress-strain curves and failure morphologies were analyzed to assess their mechanical behavior and compare them with the computational predictions.

3.4 FEA and Experimental Results of the Optimized Tensile and Compression Specimens

Figure 10 presents the finite element results for the equivalent stress distribution in the optimized tensile and compression specimens. Variations in the stress magnitude were observed along the specimens as a consequence of the lattice topology.

In Figure 10a, the principal stress concentration zone is indicated by a red arrow. Stress levels in this region were significantly higher than those in surrounding areas, corresponding to locations where fracture initiation was experimentally observed. The local reduction in wall thickness in these regions led to higher stress and served as preferential sites for crack initiation. This reduction is a direct consequence of the 50% mass-retention constraint applied during topology optimization, which redistributed material from low-stress areas while thinning the load-bearing lattice trusses.

Several regions of reduced strength were identified at the thin walls and at the truss lattice. Furthermore, specific areas exhibited safety factor values between 1.4 and 2.0, mainly influenced by the orientation of the applied load relative to the lattice structure (Figure 10b).

Similar behaviors were identified when comparing the non-optimized and optimized specimens: both exhibited stress concentration in analogous regions; however, the optimized specimens displayed more pronounced stress gradients due to the reduced infill volume. These results demonstrate that the numerical model accurately

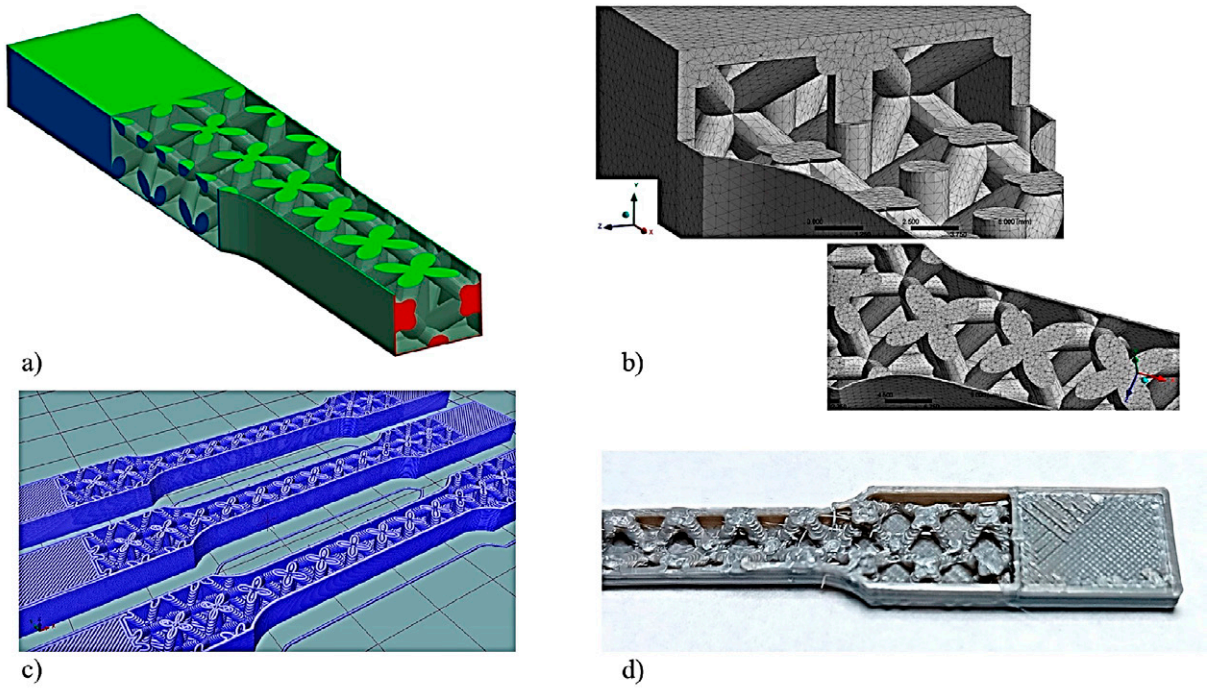

Figure 8. Topology-optimized tensile specimen. a) CAD model, b) generated mesh, c) preview of a G-code layer, and d) 3D printed sample (longitudinal section).

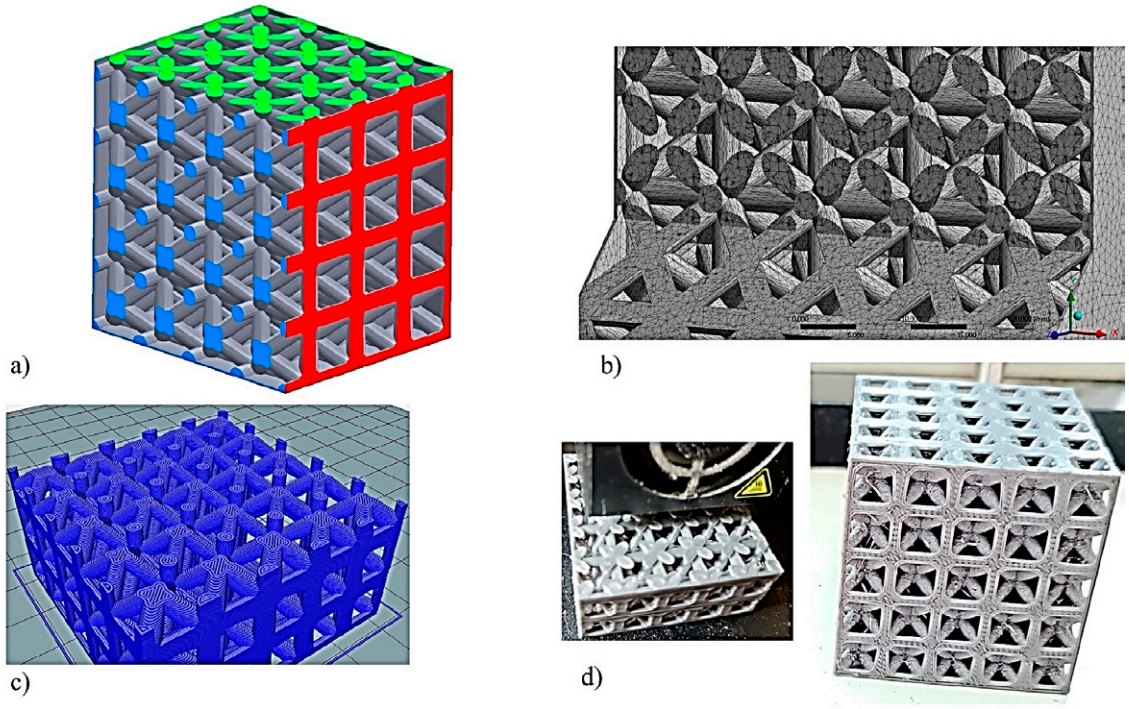

Figure 9. Topology-optimized compression specimen. a) CAD model, b) generated mesh, c) preview of a G-code layer, and d) 3D printed sample.

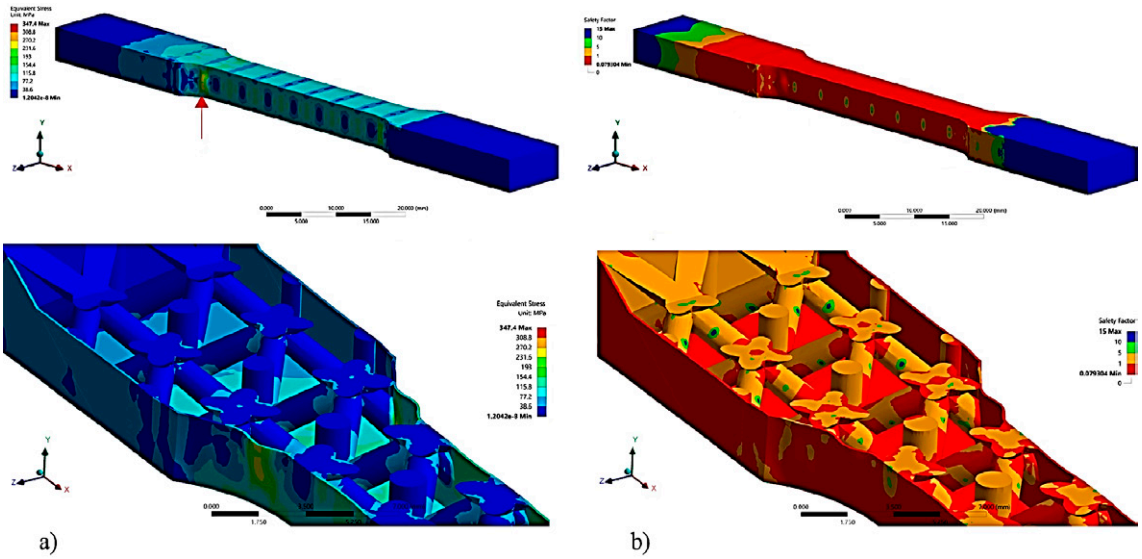

Figure 10. Tensile FEA results, topology-optimized tensile specimen. a) Equivalent stress and b) safety factor (maximum equivalent stress).

predicted the experimental failure zones, correlating the consistency between the finite element simulations and the mechanical tests. The comparison between the computed maximum loads and the experimentally measured values is presented in the following section.

The simulated results of the optimized compression specimens are presented in Figure 11, which displays the equivalent stress and safety factor contours. In this case, the optimized samples exhibited a regular mechanical response under the applied compressive load. The critical stress regions were localized along the lattice truss, which were axially aligned with the load direction. This stress distribution agrees well with the experimental observations, where the same columns exhibited visible damage after testing.

Despite localized deformation in these regions, the remaining lattice structure redistributed the applied load, demonstrating the capability of the optimized geometry to maintain structural integrity. The axial alignment of the BCC lattice columns provided an efficient load path, reducing bending effects and enabling a more uniform stress transfer through the interconnected nodes. This structural configuration explains the superior compressive behavior compared with the tensile case.

Considering the imposed 50 % mass reduction, the compressive specimens maintained a satisfactory level of mechanical resistance under the $1x10^4$ N load, confirming that the topology-optimized lattice configuration achieved a favorable balance between stiffness and lightweight design. The agreement between the numerical

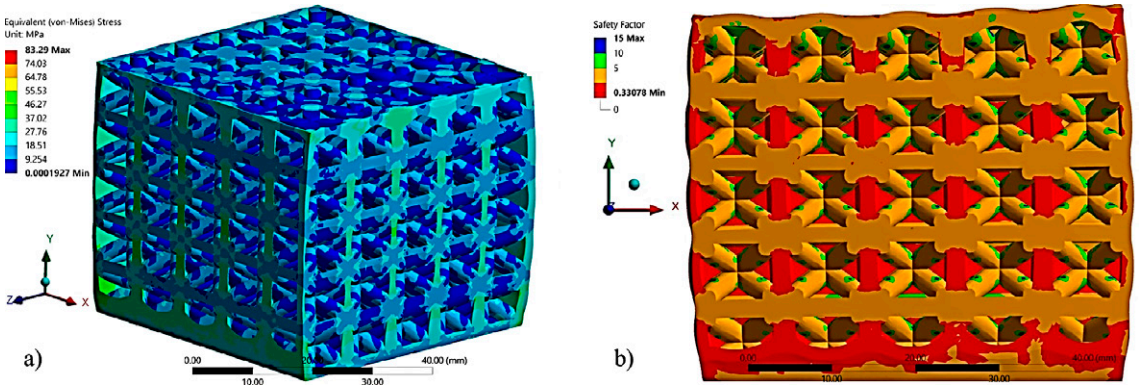

Figure 11. Compressive FEA results, topology-optimized compression specimen. a) Equivalent stress and b) safety factor (maximum equivalent stress).

and experimental stress patterns further validates the reliability of the finite element model and the predictive accuracy of the topology optimization procedure.

3.5 Compression and Tensile Test Results for Lattice-Optimized Specimens

The stress-strain curves of the optimized specimens are presented in Figures 12a and 12b. For the optimized tensile specimens (OTS), a reduction in mechanical properties was observed compared with the non-optimized tensile samples. The overall response under the applied axial load showed lower ductility, attributed to the decrease in infill percentage and the effect of lattice size. The fracture location, previously indicated by red arrows in Figure 3c and now in Figure 12c, was similar in both the optimized and the normal specimens, confirming that the topology optimization preserved the principal load path while reducing the cross-sectional area. The loss of stiffness and strength in the optimized tensile specimens can be directly associated with the thinning of the lattice bars and the limited ability of the structure to redistribute tensile stresses once local yielding occurs.

In contrast, the mechanical behavior of the optimized compression specimens (OCS) exhibited a distinctive and interesting trend. As shown in Figure 12b, the initial slope of the curve is steeper than that of the non-optimized compression specimens, indicating a higher initial stiffness and improved load-bearing efficiency. This enhancement can be explained by the axial alignment of the BCC lattice columns with the applied compressive load, which facilitates direct stress transfer and delays global instability. However, after reaching the elastic limit, the mechanical properties decreased gradually. The plateau region, highlighted by a red arrow, represents a stage of progressive reorientation and local collapse of the lattice truss, followed by the beginning of plastic deformation.

This behavior suggests that the PLA used did not exhibit the typical brittle response; instead, it demonstrated ductile-like behavior characterized by continuous yielding and energy absorption. The absence of multiple abrupt drops or irregularities in the stress-strain curve can support this interpretation. These results highlighted that the optimized lattice configurations achieved a good balance between mass reduction and mechanical performance, particularly under compression, where the optimized geometry retained most of its load-carrying capability. The corresponding mechanical properties of the optimized tensile and compression specimens are summarized in Table 2.

3.6 Load Capacity Comparison

The mechanical properties of the optimized specimens were ultimately reduced due to the ≈50% mass decrease imposed during topology optimization. For the optimized tensile specimens, the reductions with respect to the non-optimized tensile specimens were as follows: Young's modulus (E) ≈ -53 %, ultimate tensile strength (UTS) ≈ -60 %, and yield stress (σ_y) ≈ -48 %, as shown in Figure 13a. The optimized compression specimens exhibited reductions in compressive strength of ≈ -61 % and σ_Y ≈ -74 %, but an increase in stiffness of roughly +41 % relative to the non-optimized compression specimens.

A particularly relevant result of this study was the increase in the apparent initial stiffness observed in the optimized compression specimens relative to the non-optimized compression samples. This behavior indicates that the mechanical response was governed not only by the reduction in mass but also by the way in which the remaining material was redistributed by the topology optimization procedure. Under compressive loading, the BCC lattice architecture provided preferential load-transfer paths that were more effectively aligned with the loading axis, allowing a more direct transmission of the applied force during the initial deformation stage.

This result suggests that, in compression, structural efficiency may improve even when the total material amount is reduced, provided that the optimized geometry promotes stable axial force transmission and delays the onset of local instability. By contrast, under tensile loading, the same material reduction produced thinner load-bearing regions and greater stress concentration, which reduced both the apparent initial stiffness and the

Table 2. Mechanical properties of the topology-optimized tensile and compression specimens.

	Young´s modulus (GPa)	Ultimate tensile strength (MPa)	Compressive strength (MPa)	Tensile yield strength (MPa)	Compressive yield strength (MPa)
Tensile	0.0988	11	--	8.40	--
Compression	0.37486	--	5.88	--	3.8

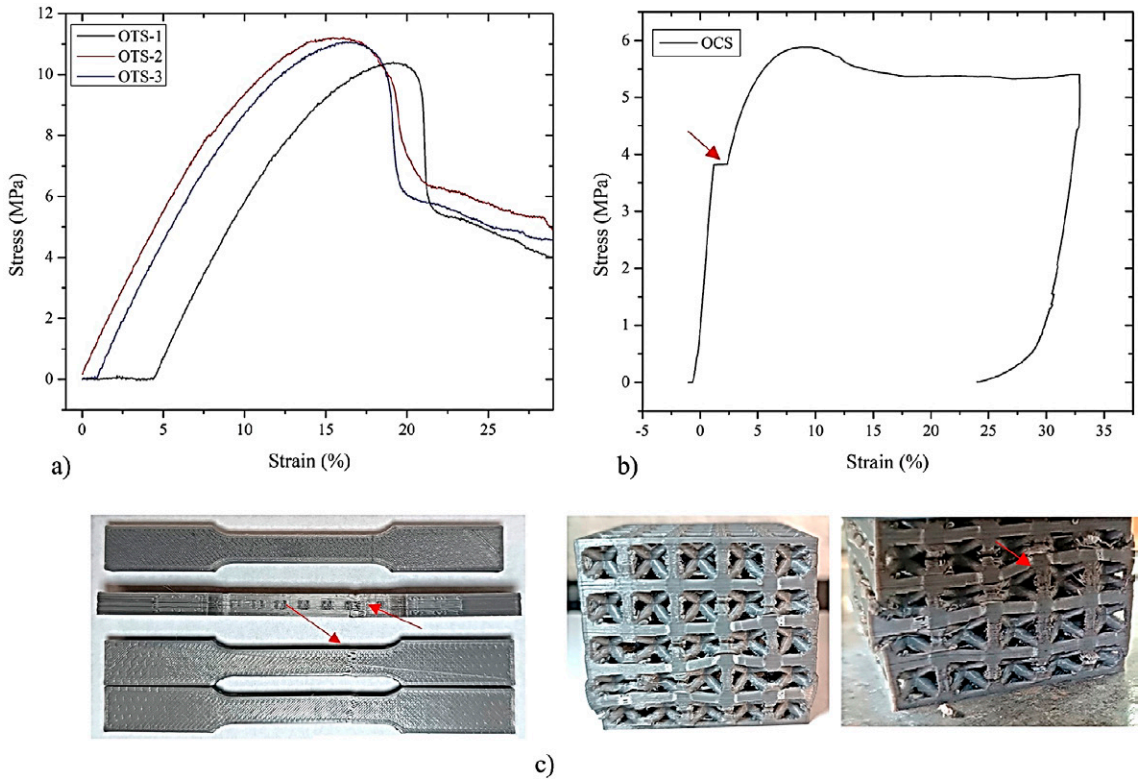

Figure 12. Stress-strain curves. a) Optimized tensile specimens, b) optimized compression specimens, and c) deformations and fractures observed in the tensile and compression specimens evaluated. Some deformed areas are indicated with red arrows.

strength. Therefore, the present results indicate that the mechanical effect of topology optimization in PLA cannot be interpreted only in terms of mass loss, since the loading mode and lattice orientation strongly influence the global load-bearing response.

Further investigations are required to confirm whether this stiffness enhancement arises from the lattice architecture, the orientation of the printed layers, or localized densification during the printing process. Figure 13b compares the mechanical properties of both compression specimens.

Regarding the boundary conditions and maximum load-bearing capacity determined by FEA, the TS supported a maximum load of approximately 826 N, whereas the OTS reached a maximum of 327 N. For compression, the non-optimized CS exhibited a maximum load of 3.82×10^4 N, and the OCS exhibited a maximum load of 1.42×10^4 N. The reduction in load capacity of the OTS is nearly proportional to the fraction of mass removed (approximately 50 %), indicating that the topology optimization produced a mechanically efficient design that retains structural functionality while significantly reducing the amount of material used. This proportionality highlights the potential of the method for lightweight component design, where predictable trade-offs between stiffness and mass are desirable.

The simulated optimized compression specimens sustain the nominal design load of 1×10^4 N without catastrophic failure, consistent with the experimental results. Both the simulation and experimental tests exhibited failure initiation at the outer lattice walls (Figures 11b and 12c), which did not significantly affect global structural performance. Consistency was observed between the numerical predictions and the experimentally observed deformation patterns, as summarized in Figure 14. Nevertheless, this validation should be interpreted as a first-order correlation, since a direct quantitative comparison between the simulated stress fields and the local damage evolution was not performed in this study. The FEA-predicted stress distribution and final deformation morphology closely matched the experimental observations, confirming the reliability of the topology optimization approach and the adequacy of the modeling assumptions.

Thus, the optimized compression specimens exhibited higher mechanical performance than the optimized

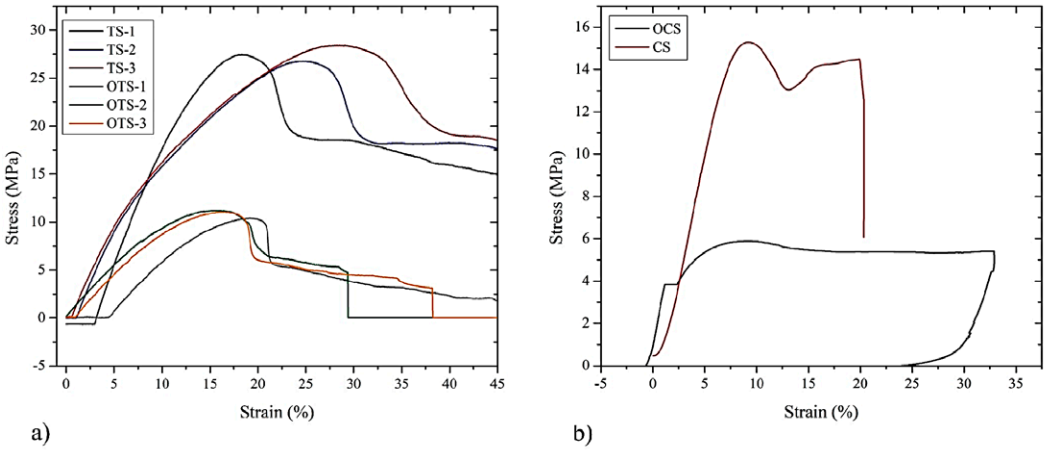

Figure 13. Stress-strain behavior for: a) tensile and b) compression tests.

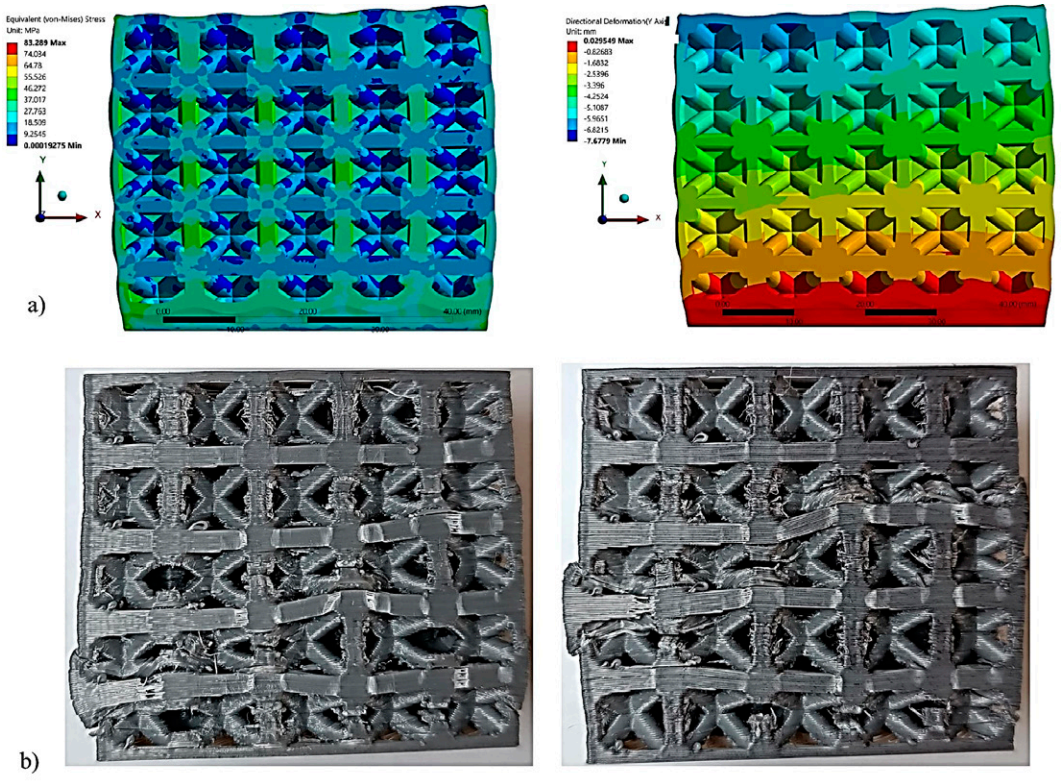

Figure 14. Comparison between: a) FEA results and b) experimental behavior obtained for the optimized compression specimen.

tensile specimens, primarily due to the larger lattice cell size and the favorable alignment of the BCC structure with the applied compressive load. This configuration enabled a more efficient load transfer through the lattice columns and improved energy absorption, mitigating premature failure.

Therefore, it can be concluded that the applied topology optimization strategy successfully achieved its design objective: a significant reduction in mass (≈ 50 %) while preserving a satisfactory level of mechanical integrity, particularly under compressive loading. The load

capacity and mass differences for all the manufactured specimens are summarized in Table 3.

It is important to mention that the relatively high Poisson's ratio obtained for the printed PLA ≈ 0.48 may be associated with the specific printed architecture generated by the FDM process, including the filament arrangement, local heterogeneity, and the thermal history of deposition. However, this value should be interpreted as an apparent Poisson's ratio under the present testing conditions, rather than as an intrinsic property of homogeneous bulk PLA. Therefore, the use of the von Mises criterion was considered an engineering approximation consistent with the observed deformable response of the printed specimens. Finally, it can be noted that the internal architecture of the non-optimized specimens was generated at a nominal infill density of 100%. Under this condition, the printed structure did not correspond to a conventional sparse infill pattern with intentionally defined internal voids, but rather to a practically filled region formed by alternating deposition lines. Therefore, although a low-density infill geometry did not govern the response, the deposited line arrangement may still have influenced the mechanical behavior of the printed specimens.

Conclusions

Lattice structures manufactured by additive manufacturing have been widely studied; fewer works have combined the experimental characterization of the printed base material, finite element analysis, topology optimization, and experimental validation under both tensile and compressive loading within a single PLA-based workflow. This practical gap motivated the present study, particularly in view of the need to assess whether mass-reduced geometries remain mechanically functional under different loading modes.

In this study, the mechanical behavior of 3D-printed PLA tensile and compression specimens was evaluated under standard and topology-optimized conditions. The base material was experimentally characterized, and the resulting mechanical properties were implemented in finite element simulations to define representative tensile and compressive loading cases. A body-centered cubic lattice topology optimization with a fixed 50% mass-retention constraint was then applied, and the optimized geometries were subsequently fabricated and mechanically tested.

The obtained results showed that the reduction in mass did not affect both loading modes in the same manner. Under tensile loading, the optimized specimens exhibited a marked decrease in strength and apparent initial stiffness, mainly associated with the reduction of the effective load-bearing section and the higher sensitivity to local stress concentration. In contrast, for compressive loading, the optimized specimens retained a more favorable structural response, which was associated with the more efficient axial load transfer provided by the selected BCC architecture. In this sense, the present findings indicate that the mechanical effect of topology optimization in PLA cannot be interpreted only in terms of mass reduction, since it also depends strongly on the loading mode and the resulting load-transfer paths within the lattice structure.

Overall, the proposed methodology proved feasible as a first-order engineering approach for the design of lightweight PLA components. The numerical and experimental results showed a qualitative consistency in the main deformation trends, although a direct quantitative comparison of local damage evolution was beyond the scope of this study. Therefore, the present work contributes to the current understanding of topology-optimized PLA structures by showing that a fixed mass-retention condition may lead to substantially different mechanical outcomes in tension and compression, and that this distinction should be considered when designing lattice-based polymer components for additive manufacturing.

Table 3. Mechanical properties as a function of load capacity. The mass of the samples is added.

	Ultimate tensile strength (N)	Ultimate compressive strength (N)	Tensile yield strength (N)	Compressive yield strength (N)	Mass (g)
Tensile	826.7	--	486	--	4
Tensile-O	327	--	252.1	--	2.8
Compression	--	$3.82x10^4$	--	$3.7x10^4$	113
Compression-O	--	$1.417x10^4$	--	$9.5x10^3$	61

Conflict of Interest

The authors declare that they have no conflicts of interest to disclose.

Funding

The authors received no specific funding for this work.

Acknowledgements

A. Monzamodeth Román-Sedano acknowledges the postdoctoral support provided by SECIHTI (CVU: 828336) and the technical assistance of H. H. Hinojosa Galvan and E. Vázquez from ICF-UNAM, G. Arámburo, S. García, I. Puente, I. Reyes from FQ UNAM, and F. Garcia, G. Lara, A. Tejeda, C. Ramos, C. Flores, and A. Pompa from IIM-UNAM.

References

Abeykoon, C., Sri-Amphorn, P., & Fernando, A. (2020). Optimization of fused deposition modeling parameters for improved PLA and ABS 3D printed structures. International *Journal of Lightweight Materials and Manufacture*, 3(3), 284–297.
https://doi.org/10.1016/j.ijlmm.2020.03.003

Gavazzoni, M., Pisati, M., Beretta, S., & Foletti, S. (2021). Multiaxial static strength of a 3D printed metallic lattice structure exhibiting brittle behavior. *Fatigue & Fracture of Engineering Materials & Structures*, 44(12), 3499–3516.
https://doi.org/10.1111/ffe.13587

Hooshmand, M. J., Sakib-Uz-Zaman, C., & Khondoker, M. A. H. (2023). Machine Learning Algorithms for Predicting Mechanical Stiffness of Lattice Structure-Based Polymer Foam. *Materials*, 16(22), 7173.
https://doi.org/10.3390/ma16227173

Mahapatra, I., Chikkanna, N., Shanmugam, K., Rengaswamy, J., & Ramachandran, V. (2025b). Evaluation of tensile properties of 3D-printed lattice composites: Experimental and machine learning-based predictive modelling. *Composites Part A Applied Science and Manufacturing*, 193, 108823.
https://doi.org/10.1016/j.compositesa.2025.108823

Bedoya, M. C., Restrepo, J. W., Wilches, L. V., & Rodriguez, J. (2025). Cellular Structures Analysis Under Compression Test. *Polymers*, 17(11), 1476.
https://doi.org/10.3390/polym17111476

Yang, J., Liu, H., Cai, G., & Jin, H. (2025). Additive Manufacturing and Influencing Factors of Lattice Structures: A Review. *Materials*, 18(7), 1397.
https://doi.org/10.3390/ma18071397

León-Becerra, J., González-Estrada, O. A., & Quiroga, J. (2021). Effect of relative density in In-Plane mechanical properties of common 3D-Printed polylactic acid lattice structures. *ACS Omega*, 6(44), 29830–29838.
https://doi.org/10.1021/acsomega.1c04295

Park, K., Min, K., & Roh, Y. (2021). Design Optimization of Lattice Structures under Compression: Study of Unit Cell Types and Cell Arrangements. *Materials*, 15(1), 97.
https://doi.org/10.3390/ma15010097

Raja, S., Agrawal, A. P., Patil, P. P., Thimothy, P., Capangpangan, R. Y., Singhal, P., & Wotango, M. T. (2022). Optimization of 3D printing process parameters of polylactic acid filament based on the mechanical test. *International Journal of Chemical Engineering, 5830869*.
https://doi.org/10.1155/2022/5830869

Monzamodeth R-SA, Nicolás Iván R-R, Bernardo H-M, Osvaldo F, Fermín C, Bernardo C. (2022). Beehive wind turbine: A new design for electric power generation in urban and semi-urban zones. *Wind Engineering*; 46(5):1427-1439.
doi:10.1177/0309524X221080573

Monzamodeth, R. A., Iván, R. N., Oscar, X., Bernardo, H., Osvaldo, F., Fermín, C., & Bernardo, C. (2021). Development of a wind turbine using 3D printing: A prospection of electric power generation from daily commute by car. *Wind Engineering*, 46(2), 376–391.
https://doi.org/10.1177/0309524x211029563

Teng, F., Sun, Y., Guo, S., Gao, B., & Yu, G. (2022). Topological and mechanical properties of different lattice structures based on additive manufacturing. *Micromachines*, 13(7), 1017.
https://doi.org/10.3390/mi13071017

Xu, Y., Han, G., Huang, G., Li, T., Xia, J., & Guo, D. (2023). Properties Evaluations of Topology Optimized Functionally Graded Lattice Structures Fabricated by Selective Laser Melting. *Materials*, 16(4), 1700.
https://doi.org/10.3390/ma16041700